Masuda's sandstone core hydrate dissociation experiment revisited

Jack S. Hardwick[a], Simon A. Mathias[a,*]

[a]*Department of Earth Sciences, Durham University, Durham, UK*

Abstract

Numerical simulation of hydrate dissociation in porous media is important to investigate future hydrate fuel extraction strategies and/or the impacts of climate change on the long-term stability of vulnerable near-surface hydrate deposits. The core-scale hydrate dissociation experiment of Masuda et al. (1999) represents an important experimental data set that can be used for benchmarking numerical simulators for this purpose. Data collected includes gas production, water production, boundary pressure and temperature from three internal observation points. At least six modeling studies exist within the literature seeking to simulate the gas production data and the temperature data. However, the pressure data and water production data are generally overlooked. In this article we present a set of numerical simulations capable of reconciling the Masuda et al. (1999) data set in its entirety. Improvements on existing modeling studies are achieved by: (1) using improved estimates of the initial hydrate saturation; (2) obtaining relative permeability parameters, a hydrate stability depression temperature and a convective heat transfer coefficient by calibration with the observed data; (3) applying a new critical threshold permeability model, specifically to reconcile a relatively fast gas production with a relatively slow far-field boundary pressure response. A subsidiary finding is that permeability is significantly reduced in the presence of very low hydrate saturations. But more importantly, the multi-faceted effectiveness of the data set from Masuda's experiment is clearly demonstrated for numerical simulation benchmarking in the future.

Keywords: Methane hydrate, Porous core, Dissociation, Depressurization, Relative permeability, Numerical simulation

1. Introduction

The ability to simulate and forecast hydrate dissociation in marine sediments is important to both improving our understanding of the possible impacts of global warming on methane release and developing efficient methodologies for industrial methane extraction as a fossil fuel resource. Many relevant numerical and experimental studies are reported in the literature, but an article of particular significance is that of Masuda et al. (1999), which presents experimental results from four core-scale experiments whereby hydrate in a sandstone is dissociated by depressurization while the outer surface of the core is exposed to a constant temperature "air-bath".

Observed data from the experiments include time-series of gas production, water production, pressure at the core boundary far-field to the fluid outlet and temperature at three different points in the core. Masuda et al. (1999) also present results from one-dimensional numerical simulations of these data from their own numerical simulator. Their model results do a good job of capturing the observed pressure response from the experiments. However, their simulated gas production is significantly delayed as compared to the observed data. Furthermore, their simulated temperature distribution bares little resemblance to the observed data and simulated water production is not reported.

Interestingly, there are at least six published independent attempts to provide and/or improve numerical simulations of these experiments (Nazridoust and Ahmadi, 2007; Liang et al., 2010;

*Corresponding author. Tel.: +44 (0)1913343491, Fax: +44 (0)1913342301, E-mail address: s.a.mathias@durham.ac.uk

Zhao et al., 2012; Ruan et al., 2012a; Shin, 2014; Chen et al., 2016). In addition to these, there are several articles reporting to explicitly use the Masuda et al. (1999) study as a base case for numerical parameter sensitivity analysis (Gamwo and Liu, 2010; Ruan et al., 2012b; Zhao et al., 2014, 2015, 2016; Song et al., 2016).

Nazridoust and Ahmadi (2007) sought to improve on the numerical work of Masuda et al. (1999) by developing a two-dimensional axisymmetric simulation of the fourth experiment presented by Masuda et al. (1999), hereafter referred to as Run 4. Nazridoust and Ahmadi (2007) performed their simulations using the commercial CFD code, FLUENT. Their simulated results provided a much better match to the observed temperature time-series and gas production data, as compared to those of Masuda et al. (1999). However, their simulated far-field boundary pressure was found to decline much earlier than the observed data. Furthermore, their predicted water production volume was 3.3 times that observed from the experiment.

The differences between the simulated results of Masuda et al. (1999) and Nazridoust and Ahmadi (2007) are unlikely to be due to using a one-dimensional or two-dimensional spatial representation. Note that a two-dimensional representation would delay heat transport from the air-bath to the center of the core, as compared to a one-dimensional representation, suggesting that Nazridoust and Ahmadi (2007) should have forecasted slower gas production as opposed to faster.

Liang et al. (2010) attempted to simulate Masuda's Run 4 data using their own IMPES (implicit pressure-explicit saturation) numerical scheme based on the governing equations for hydrate dissociation simulation previously presented by Sun et al. (2005). Their presented numerical results were similar to those of Nazridoust and Ahmadi (2007). Interestingly, Liang et al. (2010) comment on the inconsistency of the Nazridoust's simulation with Masuda's observed pressure

data, but do not present simulated pressure data of their own in this context.

Zhao et al. (2012) present results from numerical simulations that should have provided identical results to those of Liang et al. (2010). However, their temperature time-series data is very different to both Masuda's observed data and the simulation results from Liang et al. (2010). Of interest is that Zhao et al. (2012) forecasts an additional delay in the temperature decline due to the heat consumption associated with hydrate dissociation.

Another important aspect of the Masuda et al. (1999) study is that they derive, by calibrating their numerical model to their observed data, an empirical power law to describe permeability reduction as a function of hydrate saturation. The exponent of the power law was found to be 15. The numerical simulations of Nazridoust and Ahmadi (2007) and Liang et al. (2010) also adopted this empirical function. Ruan et al. (2012a) provide an additional attempt to simulate Masuda's Run 4, which yielded very similar results to those of Liang et al. (2010). However, Ruan et al. (2012a) used the same empirical function for permeability reduction but with an exponent of 11.

Shin (2014) attempted to simulate Masuda's Run 4 using an in-house finite element model. Shin (2014) only report limited information with regards to model parameterization. However, it is clear form their presented results that their model underestimates the amount of gas produced during the experiment by around 3%.

Chen et al. (2016) present simulation results for Masuda's Run 4 but only for the temperature and pressure time-series data. They also compare their numerical results directly with those of Nazridoust and Ahmadi (2007) and Zhao et al. (2012). All the numerical results look very different. The main difference between the simulation of Chen et al. (2016) and the other numerical studies discussed above is that Chen et al. (2016) applies a constant temperature boundary to the

sides of the core whereas all the other studies apply adiabatic boundary conditions, in conjunction with a heat production term associated with heat transfer from the outer constant temperature air-bath.

Of particular interest is that, with the exception of Nazridoust and Ahmadi (2007), none of the numerical studies discussed above report results concerning simulated water production. Furthermore, with the exception of Masuda et al. (1999) and Nazridoust and Ahmadi (2007), none of the above studies comment on their ability to simulate the pressure data at the far-field boundary.

Our original intention was to use one of the above modeling studies to benchmark our own numerical simulator for hydrate dissociation. It is possible to closely match the results of Ruan et al. (2012a). However, this can only be achieved by significantly increasing the convective heat transfer coefficient for the heat source associated with the constant temperature air-bath, as compared to the value originally specified by Masuda et al. (1999). Once this is achieved it is found that pressure at the far-field boundary decreases too fast and insufficient gas and water are produced at the outlet, as compared to the experimental observations of Masuda et al. (1999) (recall that Ruan et al. (2012a) does not report their simulated results for water production and pressure).

The objective of this article is to present a set of numerical simulations that better match all facets of the Masuda et al. (1999) data set, for benchmarking similar numerical models in the future. In particular, this article presents a unified set of governing equations and parameter values, which can be used to provide close correspondence to all the observed experimental data including gas production volume, water production volume, far-field boundary pressure and temperature at the three temperature observation points. This is achieved by designing a new permeability

reduction model to account for the presence of hydrate and obtaining relative permeability parameters, a hydrate stability depression temperature and a convective heat transfer coefficient by direct calibration to the observed experimental data.

The outline of this article is as follows. First the mathematical equations, associated parameters and numerical solution procedure are presented. A summary of the experimental setup is provided. Calibrated model results are then presented and compared to the experimental data along with seven similar modeling studies from the literature.

2. Data and methods

2.1. Mathematical model

Consider the presence of saline water, methane and hydrate in a homogenous and isotropic porous medium. Liquid water and gaseous methane are assumed to be immiscible. The effect of water salinity is assumed only to affect the equilibrium pressure of hydrate and the salinity of the liquid water is assumed constant. Local difference between temperatures and pressures within the different phases are assumed negligible.

Following on from these assumptions, the following mass conservation statements can be made (e.g. Masuda et al., 1999; Sun et al., 2005; Ruan et al., 2012a; Chen et al., 2017):

$$\frac{\partial G_w}{\partial t} = -\nabla \cdot \mathbf{F}_w - \frac{(M_h - M_g)}{M_h}\frac{\partial G_h}{\partial t} \tag{1}$$

$$\frac{\partial G_g}{\partial t} = -\nabla \cdot \mathbf{F}_g - \frac{M_g}{M_h}\frac{\partial G_h}{\partial t} \tag{2}$$

$$\frac{\partial G_h}{\partial t} = M_h k_d A_s (P - P_e) \tag{3}$$

and the appropriate form of the accompanying heat transport equation takes the form

$$\frac{\partial U}{\partial t} = \nabla \cdot (\kappa_E \nabla T) - \nabla \cdot (\mathbf{v} H) \tag{4}$$

where G_w [ML^{-3}], G_g [ML^{-3}] and G_h [ML^{-3}] are the mass of liquid water, gaseous methane and solid hydrate per unit volume of rock, respectively, $\mathbf{F}_w$ [$\mathrm{ML}^{-2}\mathrm{T}^{-1}$] and $\mathbf{F}_g$ [$\mathrm{ML}^{-2}\mathrm{T}^{-1}$] are the mass fluxes of liquid water and gaseous methane, respectively, $M_h = N_H M_w + M_g$, M_w (= 18.02 kg/kmol) and M_g (= 16.04 kg/kmol) are the molecular weights of hydrate, water and methane, respectively, N_H [-] is the hydrate number (which is generally assumed to be 6 for methane (Sun et al., 2005)), t [T] is time, k_d [$\mathrm{L}^{-1}\mathrm{T}$] is a dissociation constant, A_s [L^{-1}] is the interface area per unit volume between the hydrate and the fluid phases, P [$\mathrm{ML}^{-1}\mathrm{T}^{-2}$] is fluid pressure, P_e [$\mathrm{ML}^{-1}\mathrm{T}^{-2}$] is the hydrate equilibrium pressure, U [$\mathrm{ML}^{-1}\mathrm{T}^{-2}$] is the total internal energy per unit volume of rock, κ_E [$\mathrm{MLT}^{-3}\Theta^{-1}$] is the effective thermal conductivity of the composite medium, $\mathbf{v}$ [LT^{-1}] is the convection velocity, T [Θ] is temperature and H [$\mathrm{ML}^{-1}\mathrm{T}^{-2}$] is the total enthalpy per unit volume of rock.

Hereafter, the subscripts w, g, h, r indicate that given properties are for liquid water, gaseous methane, hydrate or rock matrix, respectively. The mass of components per unit volume for phase i (where $i = w, g$ or h), G_i, are further defined by

$$G_i = \phi \rho_i S_i \tag{5}$$

where ϕ [-] is the rock porosity and ρ_i [ML^{-3}] and S_i [-] are the density and saturation of phase i,

125 respectively.

126 The mass fluxes of phase *i*, $\mathbf{F}_i$, are further defined using the following modified form of Darcy's

127 law

$$\mathbf{F}_i = -\frac{\rho_i k k_{ri}}{\mu_i} \nabla P \tag{6}$$

128 where k [L^2] is the rock permeability and k_{ri} [-] and μ_i [$ML^{-1}T^{-1}$] are the relative permeability and

129 dynamic viscosity for phase *i*, respectively.

130 The total internal energy per unit volume of rock, U, is related to the total enthalpy per unit

131 volume of rock, H, by $U = H - P$. It follows that U, κ_E and $\mathbf{v}H$ can be further defined by:

$$U = H - P = G_w h_w + G_g h_g + G_h h_h + (1 - \phi)\rho_r h_r - P \tag{7}$$

132

$$\kappa_E = \phi(S_w \kappa_w + S_g \kappa_g + S_h \kappa_h) + (1 - \phi)\kappa_r \tag{8}$$

133

$$\mathbf{v}H = \mathbf{F}_w h_w + \mathbf{F}_g h_g \tag{9}$$

134 where h_i [L^2T^{-2}] and κ_i [$MLT^{-3}\Theta^{-1}$] are the enthalpy per unit mass and thermal conductivity of

135 phase *i*, respectively.

136 *2.1.1. Boundary and initial conditions*

137 The cylindrical geometry of the core along with the assumption of a homogenous and isotropic

138 porous medium enables an assumption of axial symmetry such that the problem can be solved in

139 terms of normal distance away from the gas outlet, x [L], and radial distance away from the central

140 axis of the cylinder, r [L]. The core is assumed sealed on all sides except for the outlet, which

141 releases fluid due to a fixed pressure. All boundaries are treated as adiabatic with the exception
142 of a convective heat gain due to the surrounding fixed temperature air-bath. Let L [L] and R [L]
143 be the length and radius of the core, respectively. In this way, the system of equations described
144 above can be appropriately constrained by the following initial and boundary conditions:

$$
\begin{aligned}
&P = P_I, && 0 \le x \le L, && 0 \le r \le R, && t = 0\\
&T = T_I, && 0 \le x \le L, && 0 \le r \le R, && t = 0\\
&S_g = S_{gI}, && 0 \le x \le L, && 0 \le r \le R, && t = 0\\
&S_h = S_{hI}, && 0 \le x \le L, && 0 \le r \le R, && t = 0\\
&P = P_0, && x = 0, && 0 \le r \le R, && t > 0\\
&\frac{\partial T}{\partial x} = 0, && x = 0, && 0 \le r \le R, , && t > 0\\
&F_{g,x} = 0, && x = L, && 0 \le r \le R, && t > 0\\
&F_{w,x} = 0, && x = L, && 0 \le r \le R, && t > 0\\
&\frac{\partial T}{\partial x} = 0, && x = L, && 0 \le r \le R, && t > 0\\
&F_{g,r} = 0, && 0 \le x \le L, && r = 0, && t > 0\\
&F_{w,r} = 0, && 0 \le x \le L, && r = 0, && t > 0\\
&\frac{\partial T}{\partial r} = 0, && 0 \le x \le L, && r = 0, && t > 0\\
&F_{g,r} = 0, && 0 \le x \le L, && r = R, && t > 0\\
&F_{w,r} = 0, && 0 \le x \le L, && r = R, && t > 0\\
&\frac{\partial T}{\partial r} = \frac{\lambda(T_0 - T)}{\kappa_E}, && 0 \le x \le L, && r = R, && t > 0
\end{aligned}
\tag{10}
$$

where P_I [$ML^{-1}T^{-2}$], T_I [Θ], S_{gI} [-], S_{hI} [-] are the initial values of fluid pressure, temperature, gas saturation and hydrate saturation, respectively, P_0 [$ML^{-1}T^{-2}$] is the boundary pressure at the fluid outlet, T_0 [Θ] is the temperature of the air-bath and λ [$MT^{-3}\Theta^{-1}$] is the convective heat transfer coefficient describing heat transfer from the constant temperature air-bath to the boundary of the sandstone core.

2.1.2. Recasting in terms of primary dependent variables

The four partial differential equations (PDE) to be solved for include Eqs. (1) to (4). In principle, one can solve for G_w, G_g, G_h and U. However, there is a strong inter-dependence between these variables due to the effects of pressure and temperature on fluid density. Therefore, following Goudarzi et al. (2016), it is better to solve for fluid pressure, P, temperature, T, and the mass fractions of gaseous methane and hydrate in the pore-space, z_g [-] and z_h [-], respectively, found from

$$z_i = \frac{G_i}{F} \tag{11}$$

where

$$F = G_w + G_g + G_h \tag{12}$$

and

$$z_w + z_g + z_h = 1 \tag{13}$$

It is therefore necessary to use Eqs. (1) to (4) to derive four new equations for the time derivatives of z_g, z_h, P and T.

161 Note that (Goudarzi et al., 2016)

$$\frac{\partial z_i}{\partial t} = \frac{1}{F}\left(\frac{\partial G_i}{\partial t} - z_i \frac{\partial F}{\partial t}\right) \tag{14}$$

162 where

$$\frac{\partial F}{\partial t} = \frac{\partial G_w}{\partial t} + \frac{\partial G_g}{\partial t} + \frac{\partial G_h}{\partial t} \tag{15}$$

163 Given that P, T, z_g and z_h have been chosen as the primary dependent variables, it can also be

164 said that

$$\frac{\partial F}{\partial t} = \frac{\partial F}{\partial P}\frac{\partial P}{\partial t} + \frac{\partial F}{\partial T}\frac{\partial T}{\partial t} + \frac{\partial F}{\partial z_g}\frac{\partial z_g}{\partial t} + \frac{\partial F}{\partial z_h}\frac{\partial z_h}{\partial t} \tag{16}$$

165 Substituting Eqs. (5) and (11) into Eq. (12) and rearranging further leads to

$$F = \phi\left[\frac{1}{\rho_w} + \left(\frac{1}{\rho_g} - \frac{1}{\rho_w}\right)z_g + \left(\frac{1}{\rho_h} - \frac{1}{\rho_w}\right)z_h\right]^{-1} \tag{17}$$

166 from which it can be shown that the associated partial derivatives of F are obtained as follows:

$$\frac{\partial F}{\partial z_g} = -\frac{F^2}{\phi}\left(\frac{1}{\rho_g} - \frac{1}{\rho_w}\right) \tag{18}$$

167

$$\frac{\partial F}{\partial z_h} = -\frac{F^2}{\phi}\left(\frac{1}{\rho_h} - \frac{1}{\rho_w}\right) \tag{19}$$

168

$$\frac{\partial F}{\partial P} = \frac{F\alpha_E}{\phi} \tag{20}$$

169

$$\frac{\partial F}{\partial T} = -\frac{F\beta_E}{\phi} \tag{21}$$

where

$$\alpha_E = \phi(S_w\alpha_w + S_g\alpha_g + S_h\alpha_h) + (1-\phi)\alpha_r \tag{22}$$

$$\beta_E = \phi(S_w\beta_w + S_g\beta_g + S_h\beta_h) + (1-\phi)\beta_r \tag{23}$$

and α_i and β_i are the compressibility and thermal expansivity of phase i, respectively, defined by:

$$\alpha_i = \frac{1}{\rho_i}\frac{\partial \rho_i}{\partial P} \tag{24}$$

$$\beta_i = -\frac{1}{\rho_i}\frac{\partial \rho_i}{\partial T} \tag{25}$$

Also note that

$$\frac{\partial \phi}{\partial P} = (1-\phi)\alpha_r \tag{26}$$

and

$$\frac{\partial \phi}{\partial T} = (1-\phi)\beta_r \tag{27}$$

Substituting Eqs. (7) and (9) into Eq. (4) leads to

$$\begin{aligned} &G_w\frac{\partial h_w}{\partial t} + G_g\frac{\partial h_g}{\partial t} + G_h\frac{\partial h_h}{\partial t} + (1-\phi)\rho_r\frac{\partial h_r}{\partial t} \\ &+h_w\frac{\partial G_w}{\partial t} + h_g\frac{\partial G_g}{\partial t} + h_h\frac{\partial G_h}{\partial t} + h_r\frac{\partial}{\partial t}[(1-\phi)\rho_r] - \frac{\partial P}{\partial t} \\ &= \nabla\cdot(\kappa_E\nabla T) - \mathbf{F}_w\cdot\nabla h_w - \mathbf{F}_g\cdot\nabla h_g - h_w\nabla\mathbf{F}_w - h_g\nabla\mathbf{F}_g \end{aligned} \tag{28}$$

177 Substituting the mass conservation equations, Eqs. (1) to (3), then yields

$$G_w \frac{\partial h_w}{\partial t} + G_g \frac{\partial h_g}{\partial t} + G_h \frac{\partial h_h}{\partial t} + (1-\phi)\rho_r \frac{\partial h_r}{\partial t} - \frac{\partial P}{\partial t} = \nabla \cdot (\kappa_E \nabla T) - \mathbf{F}_w \cdot \nabla h_w - \mathbf{F}_g \cdot \nabla h_g + h_D \frac{\partial G_h}{\partial t} \tag{29}$$

178 where h_D [L^2T^{-2}] represents the latent heat per unit mass of hydrate, defined by

$$h_D = \frac{(M_h - M_g)(h_w - h_h) + M_g(h_g - h_h)}{M_h} \tag{30}$$

179 Note that because the porous rock is assumed to be incompressible, $\partial[(1-\phi)\rho_r]/\partial t = 0$.

180 To write the above heat transport equation in terms of temperature and pressure, it is necessary

181 to substitute (Cengel and Boles, 2002, p. 615)

$$dh_i = c_{pi} dT + \left(\frac{1 - \beta_i T}{\rho_i} \right) dP \tag{31}$$

182 where c_{pi} [$L^2T^{-2}\Theta^{-1}$] and β_i [Θ^{-1}] are the constant pressure specific heat capacity and thermal

183 expansivity of phase *i*, respectively. Finally it can be shown that (similar to Nield and Bejan,

184 2006; Mathias et al., 2014)

$$\rho_E c_{pE} \frac{\partial T}{\partial t} - \beta_E T \frac{\partial P}{\partial t} = \frac{\partial U^*}{\partial t} \tag{32}$$

185 where

$$\frac{\partial U^*}{\partial t} = \nabla \cdot (\kappa_E \nabla T) - (c_{pw}\mathbf{F}_w + c_{pg}\mathbf{F}_g) \cdot \nabla T + (c_{pw}\mu_{JTw}\mathbf{F}_w + c_{pg}\mu_{JTg}\mathbf{F}_g) \cdot \nabla P + h_D \frac{\partial G_h}{\partial t} \tag{33}$$

and

$$\rho_E c_{pE} = G_w c_{pw} + G_g c_{pg} + G_h c_{ph} + (1-\phi)\rho_r c_{pr} \tag{34}$$

and μ_{JTi} [$M^{-1}L^{-2}\Theta$] is the Joule-Thomson coefficient, defined by

$$\mu_{JTi} = \frac{\beta_i T - 1}{\rho_i c_{pi}} \tag{35}$$

Combining Eqs. (16) and (32) then yields

$$\frac{\partial P}{\partial t} = \frac{\dfrac{\partial F}{\partial t} - \dfrac{\partial F}{\partial z_g}\dfrac{\partial z_g}{\partial t} - \dfrac{\partial F}{\partial z_h}\dfrac{\partial z_h}{\partial t} - \dfrac{1}{\rho_E c_{pE}}\dfrac{\partial U^*}{\partial t}}{\dfrac{\partial F}{\partial P} + \dfrac{\beta_E T}{\rho_E c_{pE}}\dfrac{\partial F}{\partial t}} \tag{36}$$

and

$$\frac{\partial T}{\partial t} = \frac{1}{\rho_E c_{pE}}\left(\frac{\partial U^*}{\partial t} + \beta_E T \frac{\partial P}{\partial t}\right) \tag{37}$$

where $\partial z_i/\partial t$ and $\partial U^*/\partial t$ can be found from Eqs. (14) and (33), respectively.

2.1.3. The convective heat transfer coefficient, λ

The need for a convective heat transfer coefficient, λ, within the boundary conditions provided in Eq. (10), comes about due to the presence of a rubber sleeve around the sandstone core during the experiment (Masuda et al., 1999).

Let Q [ML^2T^{-3}] be the heat flux from the outside of the sandstone core, found from

$$Q = -2\pi R L \kappa_E \left.\frac{\partial T}{\partial r}\right|_{r=R} = 2\pi R L \lambda (T - T_0) \tag{38}$$

196 Assuming heat conduction within the rubber sleeve to be quasi-steady state (Crank, 1975, p.69)

$$Q = \frac{2\pi L \kappa_s (T - T_0)}{\ln[(R + t_s)/R]} \tag{39}$$

197 where κ_s [$MLT^{-3}\Theta^{-1}$] and t_s [L] are the thermal conductivity and thickness of the rubber sleeve,
198 respectively.

199 It follows that

$$\lambda = \frac{\kappa_s}{R \ln[(R + t_s)/R]} \tag{40}$$

200 According to Robert et al. (2017), the thermal conductivity of rubber ranges between 0.016
201 W m^{-1} K^{-1} and 2.3 W m^{-1} K^{-1}. Masuda et al. (1999) do not report the thickness of the rubber
202 sleeve. However, for a different but similar set of experiments, Kono et al. (2008) state that they
203 used a rubber sleeve of 10 mm thickness. Assuming a sleeve thickness of 10 mm leads to λ values
204 ranging from of 1.90 and 272.7 W m^{-2} K^{-1}, respectively. Masuda et al. (1999) report that they
205 calculated a value of λ of 16.6 W m^{-2} K^{-1}. However, given the uncertainty about the thermal
206 conductivity of rubber, it would be appropriate to treat λ as a calibration parameter in this context.
207 Note that Chen et al. (2016) applied values ranging from 80 W m^{-1} K^{-1} and 400 W m^{-2} K^{-1} for
208 their sensitivity analysis in this context.

209 *2.1.4. Relative permeability*

210 There are many articles available seeking to improve our understanding with regards to the
211 effect of hydrate on the relative permeability of gas and water (see Delli and Grozic, 2013, and
212 references therein). Here a very simple approach is adopted. When calibrating their model to

the experimental data, Masuda et al. (1999) found it necessary to assume that permeability was a power law of hydrate saturation, S_h, with a permeability reduction exponent of 15. A significant challenge was for Masuda et al. (1999) to find a model that produced most of the gas within 200 minutes whilst maintaining a significant pressure difference between the fluid outlet and the opposite end of the core throughout the experiment (see Fig. 7 of Masuda et al. (1999)). The boundary at the opposite end of the core (i.e., at $x = L$) is hereafter referred to as the far-field boundary.

The model of Masuda et al. (1999) did a good job of sustaining pressure at the far-field boundary but the gas production takes an additional 120 minutes as compared to the observed data (see Fig. 7 of Masuda et al. (1999)). In contrast, the model of Nazridoust and Ahmadi (2007) produced all the gas on time but the far-field pressure time-series was completely different to that observed during the experiment (see Figs. 8 and 10 of Nazridoust and Ahmadi (2007)). The models of Liang et al. (2010), Ruan et al. (2012a), Zhao et al. (2012) and Shin (2014) also did a good job of getting the time of gas production right. However, these studies do not report on simulated pressure reduction at the far-field boundary.

Chen et al. (2016) only report on simulated temperatures, in the context of Masuda's experiment. However, the far-field pressures reported from their associated sensitivity analysis were only able to simulate a sustained far-field boundary pressure difference for 125 minutes.

The pressure at the far-field boundary is sustained throughout Masuda's experiment because this represents the final point at which all the hydrate is dissociated, which happens at the end of the gas production period. A more simple way of ensuring our numerical model simulates this behavior is to assume that permeability is reduced to some significantly small value until the

hydrate saturation is completely dissociated. Following the ideas discussed by Daigle (2016), this point is described in our mathematical model as follows:

$$k = \begin{cases} k_c, & S_h > S_{hc} \\ k_c + (k_0 - k_c)\left(\dfrac{S_{hc} - S_h}{S_{hc}}\right), & 0 \leq S_h \leq S_{hc} \end{cases} \tag{41}$$

where k_0 [L^2] is the permeability of the medium when $S_h = 0$ and S_{hc} is a threshold value of hydrate saturation, beyond which the permeability is reduced to a value of k_c [L^2]. Ideally S_{hc} should be set to zero. However, it is found that stable numerical simulation requires $S_{hc} > 0$. A value of $S_{hc} = 10^{-4}$ is found to be sufficiently small so as not to significantly affect simulation results. The reduced permeability, k_c, is assumed to be 100 times less than k_0.

In addition to this, the relative permeability of water and gaseous methane are assumed to follow the so-called Corey curves:

$$k_{rw} = \left(\frac{S_w - S_{wr}}{1 - S_{wr}}\right)^{n_w}, \quad S_{wr} \leq S_w \leq 1 \tag{42}$$

$$k_{rg} = \left(\frac{S_g}{1 - S_{wr}}\right)^{n_g}, \quad 0 \leq S_g \leq 1 - S_{wr} \tag{43}$$

where S_{wr} [-] is the residual water saturation and n_w [-] and n_g [-] are empirical exponents.

2.1.5. Auxiliary equations and parameters

Due to the earlier assumption that liquid water and gaseous methane are assumed immiscible, only pure-component fluid properties are required. Following Mathias et al. (2014), these are obtained using the National Institute of Standards and Technology's online NIST Chemistry Web-

Book developed by Lemmon et al. (2013). Parameters available from the web book include ρ_i, c_{pi}, μ_i, κ_i and μ_{JTi} in addition to the constant-volume specific heat capacity, c_{vi} [$L^2T^{-2}\Theta^{-1}$]. Invoking the Maxwell relations, the compressibility, α_i, and thermal expansivity, β_i, can be obtained from (see Cengel and Boles, 2002, p. 627)

$$\alpha_i = \frac{T\beta_i^2}{\rho_i(c_{pi} - c_{vi})} \tag{44}$$

$$\beta_i = \frac{\rho_i c_{pi}\mu_{JTi} + 1}{T} \tag{45}$$

Intensive lookup tables can be developed for the two fluids for a wide range of temperatures and pressures prior to running a numerical solution. These can then be linearly interpolated during numerical solution of the above set of PDEs.

Following Masuda et al. (1999), the rock and hydrate are assumed to be incompressible such that $\alpha_r = \beta_r = \alpha_h = \beta_h = 0$. From Table 3 of Masuda et al. (1999) the following additional values for rock and hydrate are assumed: $c_{pr} = 800$ J kg^{-1} K^{-1}, $\kappa_r = 8.80$ W m^{-1} K^{-1}, $\rho_r = 2650$ kg m^{-3}, $c_{ph} = 2010$ J kg^{-1} K^{-1}, $\kappa_h = 0.393$ W m^{-1} K^{-1}. From Selim and Sloan (1989), $\rho_h = 913$ kg m^{-3}.

To determine the hydrate stability pressure, P_e (Pa), the empirical equation of Moridis (2002) is used

$$P_e = 10^6 \exp\left(\sum_{n=0}^{5} a_n (T + T_d)^n\right) \tag{46}$$

where

$$a_0 = -1.94138504464560 \times 10^5$$

$$a_1 = 3.31018213397926 \times 10^3$$

$$a_2 = -2.25540264493806 \times 10^1$$

$$a_3 = 7.67559117787059 \times 10^{-2}$$

$$a_4 = -1.30465829788791 \times 10^{-4}$$

$$a_5 = 8.86065316687571 \times 10^{-8}$$

where T_d (K) is a hydrate stability depression temperature associated with hydrate inhibitors such as salinity.

The brine used by Masuda et al. (1999) is reported to have a salinity of 10 ppt. Considering data presented in Fig. 7 of Wright et al. (1999) for hydrate stability in brine saturated sand and silt, it is speculated that T_d could range from 0.5 to 1.5 K for the experimental conditions of Masuda et al. (1999).

In a recent empirical study, Gupta et al. (2008) showed that an accurate estimation of the latent heat of hydrate can be obtained from the Clayperon equation. Considering again Eq. (30), the Clayperon equation (Cengel and Boles, 2002, p. 610) reveals that the latent heat of hydrate, h_D, can be found from

$$h_D = \frac{dP_e}{dT} T \left[\frac{(M_h - M_g)\left(\rho_w^{-1} - \rho_h^{-1}\right) + M_g\left(\rho_g^{-1} - \rho_h^{-1}\right)}{M_h} \right] \tag{47}$$

and assuming Eq. (46),

$$\frac{dP_e}{dT} = \left(\sum_{n=1}^{5} n a_n (T + T_d)^{n-1} \right) P_e \tag{48}$$

For the hydrate dissociation rate constant, k_d, Masuda et al. (1999) employed an empirical equation due to Kim et al. (1987). However, Clarke et al. (2001) revisited the study of Kim et al. (1987) and presented a revised empirical equation as follows

$$k_d = k_{d0} \exp\left(-\frac{\Delta E}{RT}\right) \tag{49}$$

where $k_{d0} = 36$ kmol m^{-2} Pa s and $\Delta E/R = 9572.73$ K.

Following Masuda et al. (1999)

$$A_s = \phi S_h A_{geo} \tag{50}$$

where A_{geo} [L] is the surface area to volume ratio of the hydrate particles. The diameter of the hydrate particles studied by Clarke et al. (2001) were approximately 8 μ m. Assuming the particles to be spherical, this gives a value of $A_{geo} = 6/(8 \times 10^{-6}) = 7.5 \times 10^5$ m.

Note that, following Masuda et al. (1999), Nazridoust and Ahmadi (2007), Shin (2014), Liang et al. (2010), Ruan et al. (2012a), Zhao et al. (2012) and Chen et al. (2016), Knudsen diffusion is not explicitly considered. Such an effect is unlikely to be very significant because of the relatively high pressures associated with Masuda's experiments. However, for lower pressure scenarios further consideration should be given in this respect.

2.1.6. Numerical solution

Following Mathias et al. (2014) and Goudarzi et al. (2016), the above set of equations are solved using a method of lines approach. The spatial domain is discretized into N_x equally-spaced points in the x direction and N_r equally-spaced points in the y direction using Godunov's method

(LeVeque, 1992). The resulting set of non-linear coupled ordinary differential equations with respect to time are then solved simultaneously using MATLAB's stiff solver, ODE15s (Shampine and Reichelt, 1997). No manual choice of time-step is required because ODE15s uses an adaptive time-grid to ensure numerical solution is achieved to a consistently high accuracy. For all the simulations conducted in this article, $N_x = 100$ and $N_r = 20$.

Axisymmetric problems often require extensive grid refinement in radial direction at the origin when applying source terms at $r = 0$. However, in this case, the $r = 0$ boundary is a zero flux boundary, which by its nature is very smooth. Consequently the model quickly achieves numerical convergence with increasing grid resolution. Numerical convergence was verified by comparing results from additional simulations using $N_x = 50$ and $N_r = 10$. Results from the two sets of simulations were found to be virtually identical.

2.2. Summary of the experiments

The experiments of Masuda et al. (1999) involved emplacing a mixture of water, methane and hydrate within a cylindrical core of Berea sandstone. A fixed pressure reduction was applied at one end of the core to form a fluid outlet. All other external surfaces were sealed. The core was heated during the experiment using a constant temperature air-bath. Pressure was monitored at the opposite end to the fluid outlet. Temperature was monitored at three different points within the core, T_1, T_2 and T_3. According to Fig. 1 of Masuda et al. (1999), T_1, T_2 and T_3 are located 225 mm, 150 mm and 75 mm from the fluid outlet.

The volume of methane produced from the core was recorded throughout the experiment. The total volume of water produced was recorded at the end of the experiment. Masuda et al.

Table 1: Summary of the four hydrate dissociation experiments according to Masuda et al. (1999). Note that the initial gas saturation, $S_{gI} = 1 - S_{wI} - S_{hI}$.

Run number	1	2	3	4
Air-bath temperature, T_0 (K)	275.15	275.15	275.15	275.15
Initial temperature, T_I (K)	275.45	275.45	275.45	275.45
Boundary pressure, P_0 (MPa)	3.28	3.14	2.99	2.84
Initial pressure, P_I (MPa)	3.75	3.70	3.57	3.75
Initial hydrate saturation, S_{hI} (-)	0.354	0.394	0.425	0.443
Initial water saturation, S_{wI} (-)	0.455	0.308	0.348	0.351
Volume of gas produced, V_{gP} (Scm^3)	7276	8096	8734	9106
Volume of water produced, V_{wP} (Scm^3)	6.3	6.5	12.0	11.7

(1999) repeated the experiment on the same core, four times but with different initial and boundary pressures. The various measured parameters associated with these four runs are listed in Table 1.

The length of core was, $L = 30$ cm. The cross-sectional area of the core was $\pi R^2 = 20.3$ cm^2. The absolute permeability of the core was $k_0 = 9.67 \times 10^{-14}$ m^2. The porosity of the core was $\phi = 0.182$. The methane gas was close to pure. The water had a salinity of 10 ppt. A schematic diagram of the experimental setup is presented in Fig. 1.

2.2.1. Initial hydrate saturations revisited

The initial saturations of water, gas and hydrate were determined by material balance. Of note is that Masuda et al. (1999) report that they were concerned that the estimated hydrate saturations were significantly underestimated. It is possible to explore this further by performing a material balance based on the data provided in Table 1.

The following mass balance equations can be used to relate the mass of water and methane residing in the pore-space of the sandstone core at the beginning and end of the experiment with

the masses of water and methane produced from the core by the end of the experiment:

$$m_{whI} + m_{wI} = m_{w0} + m_{wP} \tag{51}$$

$$m_{ghI} + m_{gI} = m_{g0} + m_{gP} \tag{52}$$

where m_{whI} [M] is the mass of water initially present in hydrate within the pore-space, m_{wI} [M] is the mass of liquid water present within the pore-space, m_{w0} [M] is the mass of liquid water present within the pore-space at the end of the experiment and m_{wP} [M] is the mass of liquid water produced from the core by the end of the experiment. The symbols in Eq. (52) represent identical items to those in Eq. (51) but for methane as opposed to water.

Note that:

$$m_{whI} = \frac{(M_h - M_g)\rho_h V_T S_{hI}}{M_h} \tag{53}$$

$$m_{ghI} = \frac{M_g \rho_h V_T S_{hI}}{M_h} \tag{54}$$

$$m_{wI} = \rho_{wI} V_T S_{wI} \tag{55}$$

$$m_{gI} = \rho_{gI} V_T S_{gI} \tag{56}$$

where V_T is the total pore-volume, found from

$$V_T = \pi R^2 L \phi \tag{57}$$

and S_{hI} [-], S_{wI} [-] and S_{gI} [-] represent the initial saturations of hydrate, liquid water and gaseous

methane and ρ_{wI} [ML^{-3}] and ρ_{gI} [ML^{-3}] are the densities of water and methane in the sandstone core at the initial pressure and temperature conditions.

Furthermore,

$$m_{wP} = V_{wP}\rho_{wP} \tag{58}$$

$$m_{gP} = V_{gP}\rho_{gP} \tag{59}$$

where V_{wP} [L^3] and V_{gP} [L^3] are the volumes of water and methane produced from the core at standard conditions and ρ_{wP} [ML^{-3}] and ρ_{gP} [ML^{-3}] are the densities of water and methane at standard conditions (0.1014 MPa and 15.56 ^{o}C), respectively.

At the end of the experiment it can be assumed that there is no hydrate present such that

$$m_{g0} = (V_T - m_{w0}/\rho_{w0})\rho_{g0} \tag{60}$$

and ρ_{w0} [ML^{-3}] and ρ_{g0} [ML^{-3}] are the densities of water and methane in the sandstone core at the final pressure and temperature conditions.

Substituting Eqs. (52) to (60) into Eq. (51), Eq. (51) can be solved to obtain the volume of gas produced:

$$\begin{aligned} V_{gP} = \; & \left[\left(\frac{\rho_h}{M_h}\left(\rho_{g0}\left(M_h - M_g\right) + \rho_{w0}M_g\right) - \rho_{w0}\rho_{gI}\right)S_{hI}\right. \\ & +\rho_{w0}\rho_{gI}\left(1 - S_{wI}\right) + \rho_{g0}\rho_{wI}S_{wI} - \rho_{g0}\rho_{w0} \\ & \left.-\frac{\rho_{g0}\rho_{wP}V_{wP}}{V_T}\right](\rho_{w0}\rho_{gP})^{-1} \end{aligned} \tag{61}$$

or for the volume of water produced:

$$\begin{aligned} V_{wP} = & \left[\left(\frac{\rho_h}{M_h}\left(\rho_{g0}\left(M_h - M_g\right) + \rho_{w0}M_g\right) - \rho_{w0}\rho_{gI}\right)S_{hI}\right. \\ & +\rho_{w0}\rho_{gI}\left(1 - S_{wI}\right) + \rho_{g0}\rho_{wI}S_{wI} - \rho_{g0}\rho_{w0} \\ & \left.-\frac{\rho_{w0}\rho_{gP}V_{gP}}{V_T}\right]\left(\rho_{g0}\rho_{wP}\right)^{-1} \end{aligned} \tag{62}$$

or alternatively, Eq. (51) can be solved for initial hydrate saturation:

$$\begin{aligned} S_{hI} = & \left[\rho_{g0}\rho_{w0} - \rho_{w0}\rho_{gI}\left(1 - S_{wI}\right) - \rho_{g0}\rho_{wI}S_{wI}\right. \\ & \left.+\frac{1}{V_T}\left(\rho_{g0}\rho_{wP}V_{wP} + \rho_{w0}\rho_{gP}V_{gP}\right)\right] \\ & \left[\frac{\rho_h}{M_h}\left(\rho_{g0}\left(M_h - M_g\right) + \rho_{w0}M_g\right) - \rho_{w0}\rho_{gI}\right]^{-1} \end{aligned} \tag{63}$$

Table 2 provides the values of initial, final and produced water and methane densities for the four experimental runs, based on the pressures and temperatures provided in Table 1, along with estimates of volumes of gas produced, volumes of water produced and initial hydrate saturations calculated using Eqs. (61), (62) and (63), respectively. The fact that the V_{gP} values in Table 2 are much lower than those observed by Masuda et al. (1999), reported in Table 1, confirms Masuda et al.'s concern that their estimates of S_{hI} are too low. In fact, forcing their reported values of V_{gP} and S_{hI} together, from Table 1, leads the material balance to forecast negative values for water production, V_{wP}. It is proposed that new estimates of S_{hI} in Table 2 are more accurate because they are calculated directly from the observed gas and water production values given in Table 1, using Eq. (63) and are used for all the numerical simulations conducted hereafter.

Table 2: Material balance study, determined using the pressures and temperatures in Table 1 and Lemmon et al. (2013). Following Ahmed (2001), standard conditions are assumed to be 0.1014 MPa and 15.56 ^{o}C. The volume of gas produced was calculated using Eq. (61) with all other parameters taken from Table 1. The volume of water produced was calculated using Eq. (62) with all other parameters taken from Table 1. The initial hydrate saturation was calculated using Eq. (63) with all other parameters taken from Table 1.

Run number	1	2	3	4
Initial methane density, ρ_{gI} (kg m^{-3})	28.72	28.30	27.22	28.72
Final methane density, ρ_{g0} (kg m^{-3})	24.87	23.72	22.51	21.30
Standard methane density, ρ_{gP} (kg m^{-3})	0.6789	0.6789	0.6789	0.6789
Initial water density, ρ_{wI} (kg m^{-3})	1002	1002	1002	1002
Final water density, ρ_{w0} (kg m^{-3})	1002	1001	1001	1001
Standard water density, ρ_{wP} (kg m^{-3})	999.0	999.0	999.0	999.0
Volume of gas produced, V_{gP} (Scm^3)	6411	7269	7640	8097
Volume of water produced, V_{wP} (Scm^3)	-17.4	-17.2	-21.1	-20.5
Initial hydrate saturation, S_{hI} (-)	0.403	0.441	0.487	0.501

2.3. Model calibration and validation

Following the discussion above, their remain five unknown model parameters: S_{wr}, n_w and n_g from the relative permeability functions; the hydrate stability depression temperature, T_d, associated with the salinity in the water and the porous structure associated with the sandstone; and the convective heat transfer coefficient, λ. There is a known strong correlation between S_{wr} and n_w. Therefore, S_{wr} is hereafter, somewhat arbitrarily, fixed to 0.1. Values for the other four parameters have been obtained by calibrating the mathematical model above to the observed gas production, water production, pressure and temperature data from Run 4 of Masuda et al. (1999). Run 4 is selected for comparison with earlier modelling studies (Nazridoust and Ahmadi, 2007; Liang et al., 2010; Ruan et al., 2012a; Zhao et al., 2012; Shin, 2014; Chen et al., 2016). Calibration is achieved by minimizing the following objective function

$$\varepsilon = \varepsilon_g + \varepsilon_w + \varepsilon_p + \varepsilon_{T_1} + \varepsilon_{T_2} + \varepsilon_{T_3} \tag{64}$$

where

$$\varepsilon_i = \frac{\sum_{j=1}^{N_i}(o_{ij} - m_{ij})^2}{\sum_{j=1}^{N_i}(o_{ij} - \overline{o}_{ij})^2} \tag{65}$$

and o_{ij} are observed experimental data, m_{ij} are corresponding model results, N_i are the number of observed data, $\overline{o}_{ij}$ represents the mean of the observed data, and $i = g$ for the gas production volume, $i = w$ for the final produced water volume, $i = p$ for the far-field boundary pressure, and $i = T_1, T_2, T_3$ for the observed temperature data at 225 mm, 150 mm and 75 mm from the fluid outlet, respectively.

The above objective function is minimized using MATLAB's nonlinear minimization routine, FMINSEARCH. Based on the above discussion and some preliminary simulation results, seed values (for FMINSEARH) for n_w, n_g, T_d and λ were taken to be 1.0, 2.2, 0.5 K and 50 W m^{-2} K^{-1}, respectively. As a validation exercise, Masuda's Run 2 and Run 3 are subsequently simulated using the calibrated model parameters from Run 4.

3. Results and discussion

Following calibration of the above mathematical model to the observed data from Masuda's Run 4, it was found that optimal values of n_w, n_g, T_d and λ were 0.82, 2.11, 0.98 K and 45.4 W m^{-2} K^{-1}, respectively. These values do not necessarily represent global optimal values but rather parameter values that achieve a local minimum of our objective function around the chosen seed values.

The resulting simulated output from the model is compared to the observed data from Run 4 in Fig. 2. In Fig. 2a it can be seen that the model predicts the correct amount of final gas and water

production volumes. Simulated gas production, as compared to the observed experimental data, is delayed by around 20 minutes. In Fig. 2b, the model can be seen to accurately predict most of the far-field boundary pressure data, with the exception of a mini-peak in pressure observed in the experimental data at around 50 minutes.

In Fig. 2c, it can be seen that the model does a good job of predicting the temperature data at 225 mm and 75 mm from the fluid outlet. However, there are some significant discrepancies between the model and observed data during the first 100 minutes at 150 mm from the fluid outlet.

Fig. 2d shows simulated vertically averaged hydrate saturation as a function of distance from the outlet. Here it can be seen that, even at 200 minutes, for distances from the outlet greater than 5 cm, the hydrate saturation is well over the threshold value of 10^{-4} used in the permeability model (recall Eq. (41)). Also of note is that all the hydrate is dissociated after 300 minutes.

Figs. 3 and 4 compare model and experimental results for Masuda's Runs 2 and 3, respectively, both using optimal model parameters derived from the Run 4 calibration, described above. For both Runs 2 and 3, the model underestimates far-field boundary pressure during the early part of the experiments and then overestimates the pressure in the latter part of the experiments. Water production is underestimated in Runs 2 and 3 by around 15%. However, for Run 3, the model does an excellent job of predicting the gas production data in conjunction with the temperature data at all three observation points. It was found that only minor improvement was achieved by directly calibrating the model to Runs 2 and 3 independently.

3.1. Comparison with earlier modeling studies

Fig. 5a compares our simulated far-field boundary pressure for Run 4 with model results from Masuda et al. (1999), Nazridoust and Ahmadi (2007) and Chen et al. (2016). Recall that the other modeling studies discussed above do not report their simulated far-field boundary pressure data. Our model results correspond much better to the observed far-field boundary pressure data as compared to previous reported modeling attempts. The simulated pressure data from Chen et al. (2016) reaches steady state almost 200 minutes too early. The simulated pressure data from Nazridoust and Ahmadi (2007) has the wrong shape. The simulated pressure data from Masuda et al. (1999) is closer to the observed data as compared to Nazridoust and Ahmadi (2007). However, Masuda's model overestimates the pressure throughout.

Figs. 5b and 5c compare our simulated gas production for Run 4 with model results from Masuda et al. (1999), Nazridoust and Ahmadi (2007), Shin (2014), Liang et al. (2010), Ruan et al. (2012a) and Zhao et al. (2012). Recall that Chen et al. (2016) does not report their simulated gas production data. The simulations of Masuda et al. (1999) and Shin (2014) produce around 3% less gas than the other modeling studies. Furthermore, gas production from Masuda et al. (1999) is significantly delayed as compared to the observed data and the other modeling studies. Our own simulated gas production is very similar to the results generated by Nazridoust and Ahmadi (2007); both of these studies lead to slightly delayed gas production during the first 200 minutes.

Masuda's simulation is able to predict a sustained difference between far-field and fluid outlet boundaries due to their relative permeability and permeability configuration. However, the consequence is that simulated gas production is delayed. In our new model, we are able to simulate both the sustained pressure difference and the relatively fast gas production by assuming that absolute

permeability is reduced to a 100th of its original value until hydrate saturation is below 10^{-4} (recall the discussion in Section 2.1.4). This enables porous media free of hydrate to provide significantly high mobility to both gas and water whilst simultaneously blocking off the far-field boundary from the outlet boundary pressure until (almost) all the hydrate has dissociated throughout the core.

The modeling studies of Liang et al. (2010), Ruan et al. (2012a) and Zhao et al. (2012) are worth considering together because all three of these works were developed by the same research group at Dalian University of Technology. The simulated gas production data presented by Liang et al. (2010) and Zhao et al. (2012) are almost identical. They both lead to slightly delayed gas production during the first 100 minutes and then closely follow the observed experimental data thereafter. The simulated gas production of Ruan et al. (2012a) is around 20 minutes faster than the observed experimental data. The reason for this is that both Liang et al. (2010) and Zhao et al. (2012) adopt a permeability reduction exponent of 15 (recall the discussion at the beginning of section 2.1.4) whereas Ruan et al. (2012a) adopt an exponent of 11, allowing the gas to be more mobile earlier on in the experiment.

Fig. 6 compares all the above modelling studies in terms of their ability to simulate the experimentally observed temperature data within the core at 225 mm, 150 mm and 75 mm from the fluid outlet, hereafter referred to as T_1, T_2 and T_3, respectively. All the modeling studies, with the exception of Shin (2014) and Chen et al. (2016) are able to correctly predict that T_3 declines before T_2, which declines before T_1. And similarly that T_3 rises before T_2, which rises before T_1. In contrast, Shin (2014) predicts that T_1, T_2 and T_3 decline together (Fig. 6f) and Chen et al. (2016) predicts that T_1 rises before T_2 and T_2 rises before T_3 (Fig. 6g). Interestingly, the simulated temperature responses of Liang et al. (2010) and Ruan et al. (2012a) are almost identical (compare

457 Figs. 6c and 6d). In contrast, the temperature results from Zhao et al. (2012) have a very different
458 shape, which is difficult to explain (Fig. 6e).

459 All the previous studies, with the exception of Chen et al. (2016), predict that either the min-
460 imum values of T_1, T_2 and T_3 are virtually the same or that the minimum of T_1 is less than that
461 of T_2 and that of T_2 is less than that of T_3 (Figs. 6a, and 6f). Only the Chen et al. (2016) study
462 is able to correctly predict that the minimum of T_3 is less than that of T_2 and the minimum of
463 T_2 is less than that of T_1, as observed from Masuda's experimental data (Fig. 6g). However, this
464 is at the expense of getting the order of timing wrong, as discussed in the paragraph above. Our
465 current modeling study represent a considerable improvement in model performance here because
466 our simulation gets the order correct for both the timing and the minimum values (Fig. 6h).

467 Unfortunately, none of the above studies report simulated water production volumes. How-
468 ever, assuming that these studies used the initial saturation values given in Table 1, taking their
469 final simulated gas production volumes and substituting these into Eq. (62) leads to negative val-
470 ues of water production volumes, as was seen in Table 2. This would suggest that either they
471 used different initial saturations or their equation of state for methane and water are considerably
472 different to those provided by Lemmon et al. (2013).

473 In this way it can be understood that our modeling study provides a significant improvement in
474 model performance compared to earlier studies in terms of correspondence to the various observed
475 experimental data reported previously by Masuda et al. (1999). With a single set of parameters,
476 reasonable simulations have been provided for gas production, water production, temperature and
477 boundary pressure for Masuda's Runs 2, 3 and 4 (note that experimental data for Run 1 is not
478 currently available and so this scenario has not been studied further). The reasons for the improve-

ments on earlier work are as follows: (1) improved estimates of the initial hydrate saturation have been determined by applying a material balance to the experimental data; (2) the exponents of the water and gas relative permeability (n_w and n_g) along with hydrate stability depression temperature (T_d) and the convective heat transfer coefficient (λ) have been obtained by calibrating the mathematical model to the experimental data from Run 4; (3) a critical threshold permeability model is applied, which assumes permeability is significantly reduced when hydrate saturation is greater than a critical threshold value (recall Section 2.1.4).

4. Summary and conclusions

The objective of this article was to provide a set of numerical simulations that better match the various data presented by Masuda et al. (1999) from three hydrate dissociation experiments conducted on a cylindrical core (Run 2, Run 3 and Run 4). The observed experimental data include gas production volume, water production volume, far-field boundary pressure and temperature at three temperature observation points. With the exception of Masuda et al. (1999) and Nazridoust and Ahmadi (2007), previous modeling studies in the literature only looked at gas production and temperature. None of the modeling studies in the literature discussed the ability of their models to simulate the observed water production.

A significant issue concerning the numerical simulations of Masuda et al. (1999) are that whilst their model did a good job of simulating the far-field boundary pressure, gas production was significantly delayed. In our current study it was found that a critical threshold permeability model was required to reconcile these two observations, whereby permeability for hydrate saturations $> 10^{-4}$ is assumed to be 100 times less than the absolute permeability. This enables porous media

free of hydrate to provide significantly high mobility to both gas and water whilst simultaneously blocking off the far-field boundary from the outlet boundary pressure until almost all the hydrate has dissociated throughout the core.

In addition to our new model providing good correspondence between the gas production and far-field boundary pressure data, our model is also found to be effective at simulating the water production and temperature data, improving considerably on the seven earlier modeling studies found in the literature (Masuda et al., 1999; Nazridoust and Ahmadi, 2007; Liang et al., 2010; Ruan et al., 2012a; Zhao et al., 2012; Shin, 2014; Chen et al., 2016). The reasons for the improvements on earlier work were as follows: (1) improved estimates of the initial hydrate saturation were determined by applying a material balance to the experimental data; (2) the relative permeability parameters, a hydrate stability depression temperature and a convective heat transfer coefficient were obtained by calibrating the mathematical model to the experimental data from Run 4; (3) an alternative permeability model was applied to specifically reconcile a relatively fast gas production with a relatively slow far-field boundary pressure response.

An important subsidiary finding from this work is that permeability is significantly reduced in the presence of very low hydrate saturations. The results from this analysis suggest that this phenomenon can be approximated in numerical models using a simple step function (see Section 2.1.4). It has also been shown that the initial hydrate saturations for hydrate dissociation experiments, such as those of Masuda et al. (1999), can be determined by material balance using experimentally observed volumes of produced gas and water. Finally, the multi-faceted effectiveness of the data set from Masuda's experiment is clearly demonstrated for numerical simulation benchmarking in the future.

5. References

Ahmed, T. (2001). Reservoir Engineering Handbook, Second Ed. Gulf Professional Publishing, London.

Cengel, Y. A., Boles, M. A. (2002). Thermodynamics: An Engineering Approach. Fourth Edition. McGraw and Hill.

Chen, L., Yamada, H., Kanda, Y., Lacaille, G., Shoji, E., Okajima, J., Komiya. A, Maruyama, S. (2016). Numerical analysis of core-scale methane hydrate dissociation dynamics and multiphase flow in porous media. Chemical Engineering Science, 153, 221–235.

Chen, L., Yamada, H., Kanda, Y., Okajima, J., Komiya, A., Maruyama, S. (2017). Investigation on the dissociation flow of methane hydrate cores: Numerical modeling and experimental verification. Chemical Engineering Science, 163, 31–43.

Clarke, M., Bishnoi, P. R. (2001). Determination of the activation energy and intrinsic rate constant of methane gas hydrate decomposition. The Canadian Journal of Chemical Engineering, 79(1), 143–147.

Crank, J. (1975). The Mathematics of Diffusion. Second Edition. Clarendon Press.

Daigle, H. (2016). Relative permeability to water or gas in the presence of hydrates in porous media from critical path analysis. Journal of Petroleum Science and Engineering, 146, 526–535.

Delli, M. L., Grozic, J. L. (2013). Prediction performance of permeability models in gas-hydrate-bearing sands. SPE Journal, 18(02), 274–284.

Gamwo, I. K., Liu, Y. (2010). Mathematical modeling and numerical simulation of methane production in a hydrate reservoir. Industrial & Engineering Chemistry Research, 49(11), 5231–5245.

Goudarzi, S., Mathias, S. A., Gluyas, J. G. (2016). Simulation of Three-Component Two-Phase Flow in Porous Media Using Method of Lines. Transport in Porous Media, 112(1), 1–19.

Gupta, A., Lachance, J., Sloan, E. D., Koh, C. A. (2008). Measurements of methane hydrate heat of dissociation using high pressure differential scanning calorimetry. Chemical Engineering Science, 63(24), 5848–5853.

Kim, H. C., Bishnoi, P. R., Heidemann, R. A., Rizvi, S. S. H. (1987). Kinetics of methane hydrate decomposition. Chemical engineering science, 42(7), 1645-1653.

Konno, Y., Masuda, Y., Takenaka, T., Oyama, H., Ouchi, H., Kurihara, M. (2008). Relative permeability curves during hydrate dissociation in Depressurization. In Proceedings of the 6th International Conference on Gas Hydrates

(ICGH).

Lemmon, E. E., McLinden, M. O., Friend, D. G. (2013) Thermophysical properties of fluid systems. In NIST Chemistry WebBook, NIST Standard Reference Database, vol. 69. National Institute of Standards and Technology, (online).

LeVeque, R. J. (1992), Numerical methods for conservation laws. Springer Science & Business Media.

Liang, H., Song, Y., Chen, Y. (2010). Numerical simulation for laboratory-scale methane hydrate dissociation by depressurization. Energy Conversion and Management, 51(10), 1883–1890.

Masuda, Y., Fujinaga, Y., Naganawa, S., Fujita, K., Sato, K., Hayashi, Y. (1999). Modeling and experimental studies on dissociation of methane gas hydrates in Berea sandstone cores. In 3rd International Conference on Gas Hydrates, Salt Lake City, Utah (Vol. 7, pp. 18–22).

Mathias, S. A., McElwaine, J. N., Gluyas, J. G. (2014). Heat transport and pressure buildup during carbon dioxide injection into depleted gas reservoirs. Journal of Fluid Mechanics, 756, 89–109.

Moridis, G. J. (2002). Numerical studies of gas production from methane hydrates. In SPE Gas Technology Symposium. Society of Petroleum Engineers. SPE 75691.

Nazridoust, K., Ahmadi, G. (2007). Computational modeling of methane hydrate dissociation in a sandstone core. Chemical engineering science, 62(22), 6155–6177.

Nield, D. A., Bejan, A. (2006). Convection in Porous Media. Third Edition. Springer.

Ruan, X., Song, Y., Liang, H., Yang, M., Dou, B. (2012a). Numerical simulation of the gas production behavior of hydrate dissociation by depressurization in hydrate-bearing porous medium. Energy & Fuels, 26(3), 1681-1694.

Ruan, X., Yang, M., Song, Y., Liang, H., Li, Y. (2012b). Numerical studies of hydrate dissociation and gas production behavior in porous media during depressurization process. Journal of Natural Gas Chemistry, 21(4), 381–392.

Robert R. Zarr, Josue A. Chavez, Angela Y. Lee, Geraldine Dalton, and Shari L. Young, NIST Heat Transmission Properties of Insulating and Building Materials, NIST Standard Reference Database Number 81, National Institute of Standards and Technology, Gaithersburg MD, 20899, http://srdata.nist.gov/Insulation/, (retrieved [16/06/2017]).

Selim, M. S., Sloan, E. D. (1989). Heat and mass transfer during the dissociation of hydrates in porous media. AIChE journal, 35(6), 1049–1052.

Shampine, L. F., Reichelt, M. W. (1997), The MATLAB ODE suite. SIAM Journal on Scientific Computing, 18(1), 1–22.

Shin, H. (2014). Development of a Numerical Simulator for Methane-hydrate Production. Journal of the Korean Geotechnical Society, 30(9), 67–75.

Song, Y., Wang, J., Liu, Y., Zhao, J. (2016). Analysis of heat transfer influences on gas production from methane hydrates using a combined method. International Journal of Heat and Mass Transfer, 92, 766–773.

Sun, X., Nanchary, N., Mohanty, K. K. (2005). 1-D modeling of hydrate depressurization in porous media. Transport in Porous Media, 58(3), 315–338.

Wright, J. F., Dallimore, S. R., Nixon, F. M. (1999). Influences of grain size and salinity on pressure-temperature thresholds for methane hydrate stability in JAPEX/JNOC/GSC Mallik 2L-38 gas hydrate research-well sediments. Bulletin-Geological Survey of Canada, 229–240.

Zhao, J. F., Ye, C. C., Song, Y. C., Liu, W. G., Cheng, C. X., Liu, Y., Zhang, Y., Wang, D. Y., Ruan, X. K. (2012). Numerical simulation and analysis of water phase effect on methane hydrate dissociation by depressurization. Industrial & Engineering Chemistry Research, 51(7), 3108–3118.

Zhao, J., Liu, D., Yang, M., Song, Y. (2014). Analysis of heat transfer effects on gas production from methane hydrate by depressurization. International Journal of Heat and Mass Transfer, 77, 529–541.

Zhao, J., Wang, J., Liu, W., Song, Y. (2015). Analysis of heat transfer effects on gas production from methane hydrate by thermal stimulation. International Journal of Heat and Mass Transfer, 87, 145–150.

Zhao, J., Fan, Z., Dong, H., Yang, Z., Song, Y. (2016). Influence of reservoir permeability on methane hydrate dissociation by depressurization. International Journal of Heat and Mass Transfer, 103, 265–276.

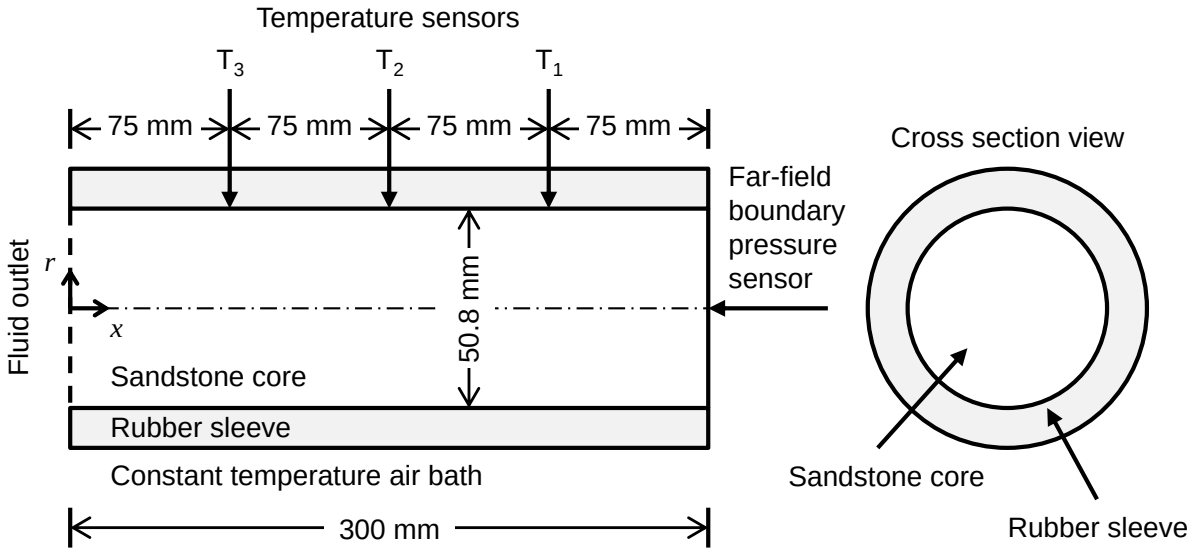

Figure 1: Schematic diagram of experimental setup (adapted from Fig. 1 of Masuda et al., 1999).

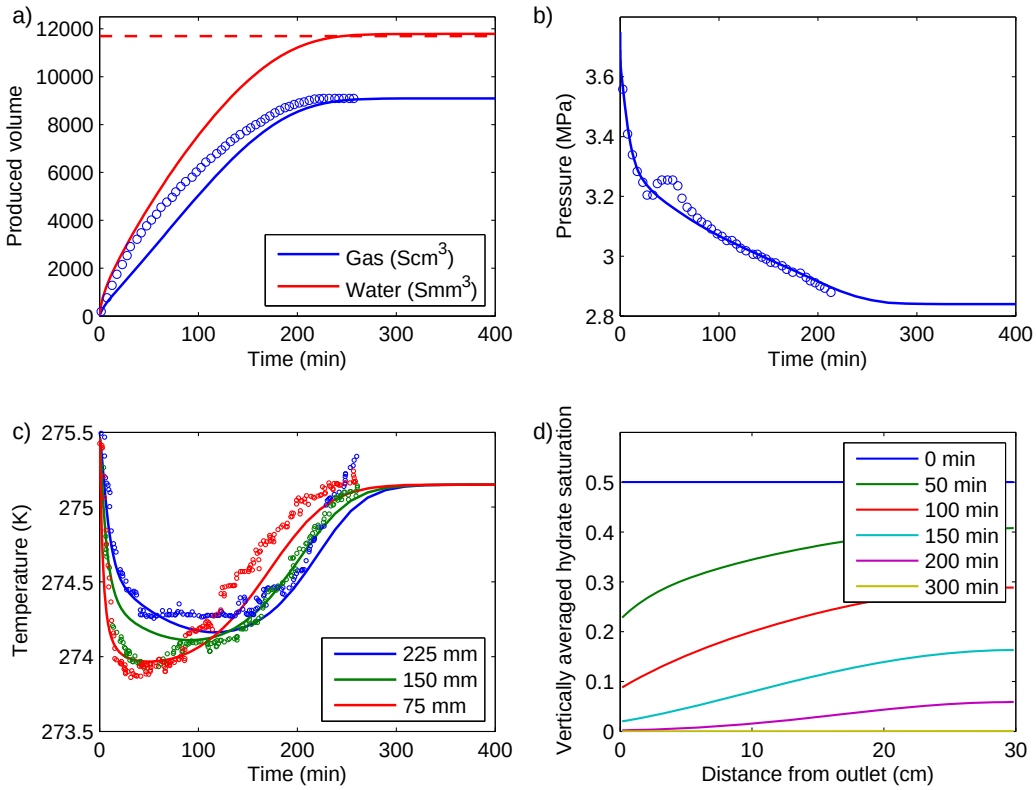

Figure 2: Comparison of the numerical model with observed data extracted from Run 4 of Masuda et al. (1999). The solid lines are from the numerical model. The circular markers are the experimental observed data from Masuda et al. (1999). a) Comparison of fluid production volumes. The dashed red line represents the experimentally observed final volume of water produced. Note that Masuda et al. (1999) do not report transient water production data. b) Comparison of far-field boundary pressures. c) Comparison of temperature data at 225 mm, 150 mm and 75 mm from the outlet boundary, respectively. All temperature measurements are assumed to be taken from the outside boundary of the cylindrical core. d) Simulated vertically averaged hydrate saturation plotted at different times as a function of distance from the fluid outlet. Note that 1 Scm^3 and 1 Smm^3 imply volumes of 1 cm^3 and 1 mm^3, respectively, at standard conditions.

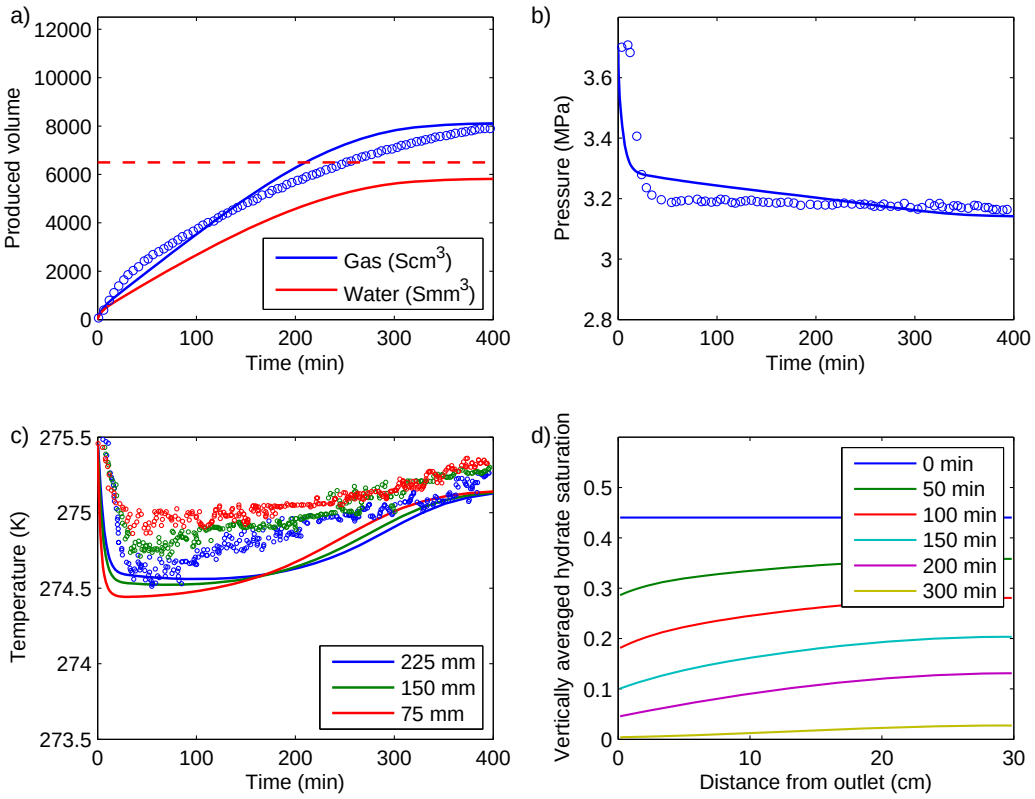

Figure 3: Same as Fig. 2 but for Run 2 of Masuda et al. (1999).

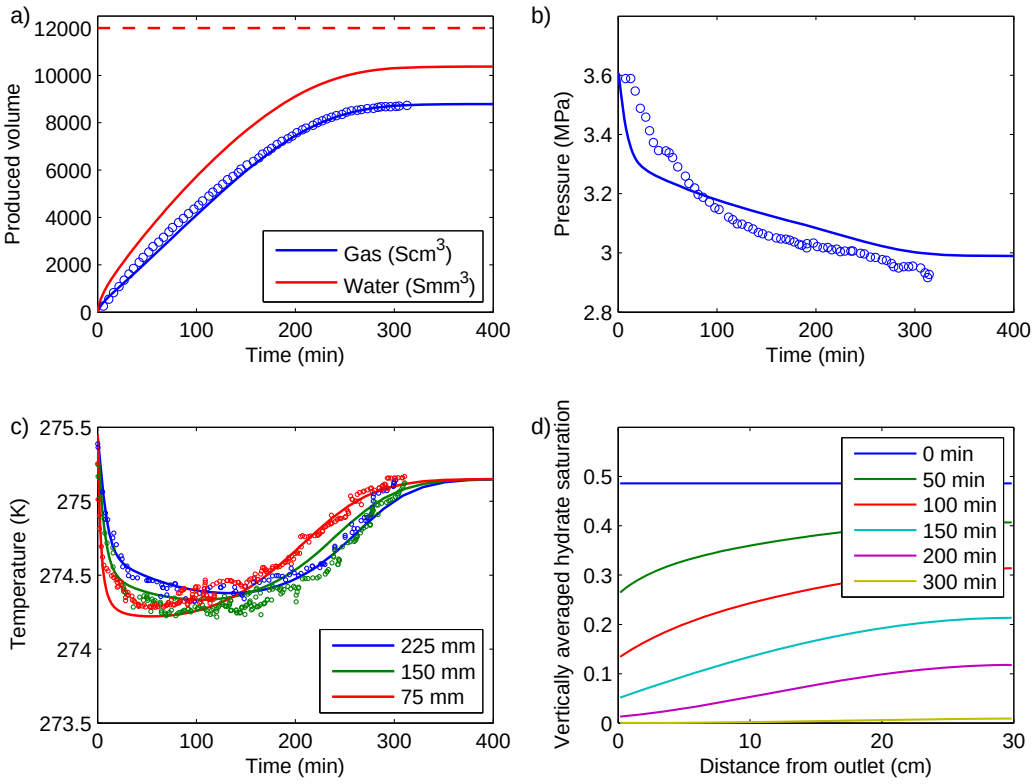

Figure 4: Same as Fig. 2 but for Run 3 of Masuda et al. (1999).

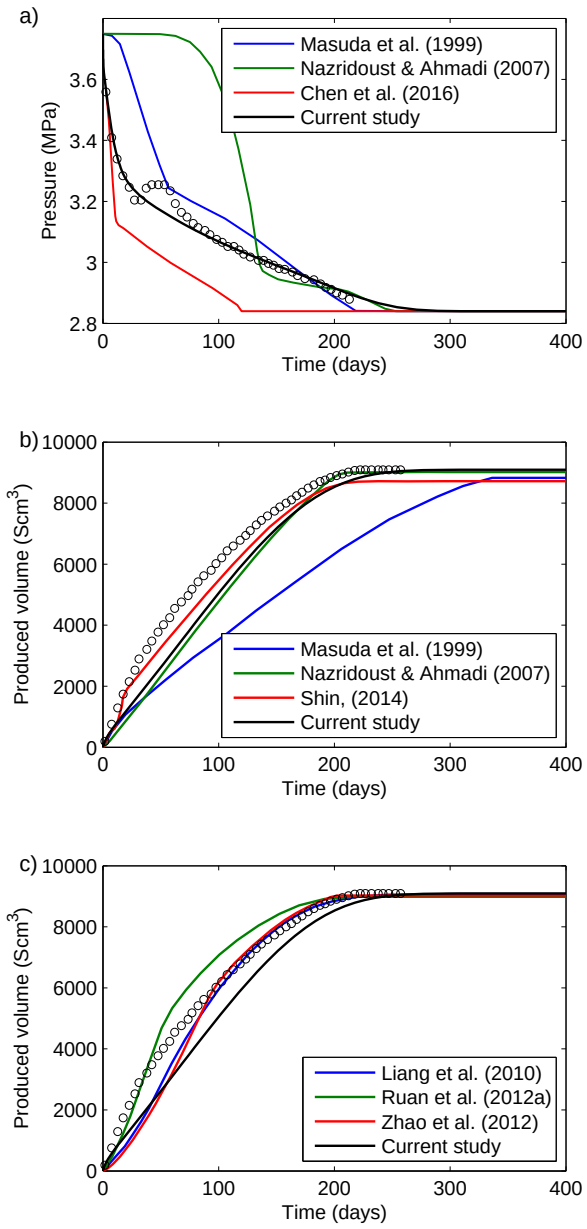

Figure 5: Comparison of far-field boundary pressure and gas production volume from different model studies in the literature along with our current study. The circular markers are the observed data extracted from Masuda et al. (1999). Note that 1 Scm^3 implies a volume of 1 cm^3 at standard conditions.

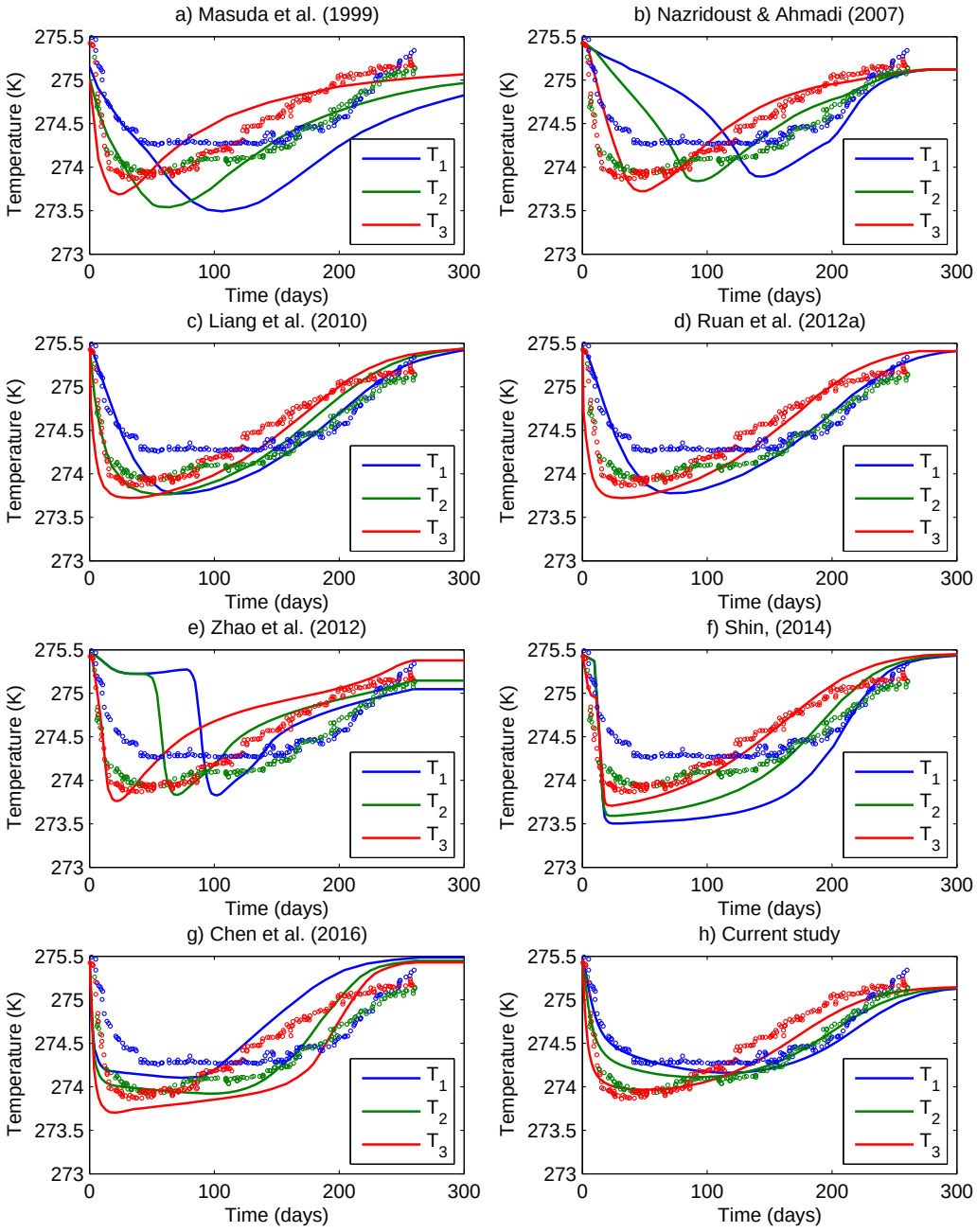

Figure 6: Comparison of temperature data from different model studies in the literature along with our current study. The circular markers are the observed data extracted from Masuda et al. (1999).